Mechanical Characteristics of Additively Manufactured ODS 316L and 316H Alloys with and without Post-Build Processing

Thak Sang Byun[1]*, Yan-Ru Lin[1], David A. Collins[1], Holden C. Hyer[1], Kelsey Epps[1], Kara Krogh[2]
[1]Oak Ridge National Laboratory, Materials Science and Technology Division, Oak Ridge, TN 37831, USA
[2]North Carolina State University, Materials Science and Engineering, Raleigh, NC 27695, USA
*corresponding author: byunts@ornl.gov

Abstract

This research aims to explore an accelerated development path for oxide dispersion strengthened (ODS) alloys by integrating additive manufacturing (AM) technologies with recent advances in ODS materials and traditional manufacturing methods. Novel AM and post-build processing routes have been developed for ODS austenitic alloys, specifically Fe-Cr-Ni alloys like 316L and 316H. Electron microscopy and mechanical characterizations were conducted to evaluate the effects of process variables on microstructure and properties, aiming for an economically feasible route property optimization. Traditionally, ODS alloy production involves multi-day high-energy mechanical milling of alloy powder with yttria (Y_2O_3), followed by powder consolidation via extrusion or other methods, and additional thermomechanical processing (TMP) for property control. To address these challenges associated with this complex and costly approach, we propose exploring alternative, cost-effective processing routes focusing on AM and traditional TMP methods. The new ODS alloy processing routes have achieved up to a 400% increase in yield strength and a 60% increase in ultimate tensile strength compared to wrought stainless steels, while still maintaining significant ductility and fracture toughness. This paper details the novel and economical AM-based processing routes for ODS austenitic alloys, combined with post-build TMPs, and discusses the mechanical and microstructural characteristics of the developed materials.

1. Introduction

The feasibility of structural materials for nuclear reactor core components is crucial for advancing nuclear energy technologies. In advanced nuclear reactors designed to achieve high thermal and economic efficiencies, these structural materials are subjected to high-temperature, high-dose neutron irradiation. Such extreme conditions significantly alter the materials' microstructure and local chemistry, leading to degradation of their mechanical, chemical, and physical properties [1]. Therefore, core components in high-performance reactors must exhibit excellent high-temperature mechanical properties, radiation resistance, and corrosion resistance, while also being feasible to manufacture. Designing and selecting these structural materials requires extensive research into viable manufacturing methods and comprehensive materials property databases. To meet the stringent performance requirements, candidate metallic alloys are typically processed to achieve fine-grained microstructures stabilized with strong and thermally stable nanoparticles, such as oxides, carbides, and nitrides [1-7].

Among advanced structural materials, oxide dispersion strengthened (ODS) alloys featuring highly stable nanoparticles such as fine oxides or oxygen-enriched nanoclusters are anticipated to play a crucial role in future fission and fusion reactor materials [8,9]. Many studies have shown that these materials, with their nanoparticle-enhanced microstructures, exhibit exceptional high-temperature stability and offer extremely high creep resistance [10,11]. The extensive interfacial area associated with such microstructural features enhances point-defect sink strength, which is beneficial for radiation tolerance and helps mitigate dimensional changes due to cavity swelling [12]. These fine, stabilized microstructures effectively trap helium atoms, forming high-density nanoscale bubbles instead of coarse bubbles at grain boundaries.

Despite the advantages offered by oxide nanoparticle-hardened microstructures in ODS alloys, the primary method for producing such microstructures remains high-energy mechanical alloying. This process can involve several days of high-energy ball milling of gas-atomized alloy powder mixed with a small amount of oxide, such as yttria (Y_2O_3), followed by consolidation through extrusion or hot isostatic pressing [5,8]. In fact, this processing route is prohibitively expensive for mass production of components and its lengthy duration makes it impractical for commercial applications. To overcome these limitations of mechanical alloying, additive manufacturing (AM) using laser melting has been proposed as an alternative method for producing ODS alloys. Our hypothesis is that the AM process is feasible for ODS alloys because the rapid local cooling after laser melting allows some oxygen content to remain in a solid-solution state, which can later precipitate into controlled oxide particles under specific thermomechanical conditions.

In general, AM technologies present numerous opportunities and challenges for constructing nuclear reactor structures. These technologies enable the design and manufacture of complex components that are often cost-prohibitive with traditional methods. Recent research has confirmed the suitability of austenitic steels for AM of complex-shaped reactor components [13-15]. This suitability is likely due to the rapid cooling during AM, which prevents the formation of the high-temperature ferrite (δ-ferrite) phase in austenitic steels during cooling, thereby avoiding degradation of mechanical properties in high-temperature service. Furthermore, the microstructures and mechanical properties of AM alloys can be tailored by adjusting processing parameters such as scan speed, laser power, powder purity, and layer thickness [16-18]. The size and orientation of fine-grained dislocation cell structures in metallic materials can particularly be controlled by varying processing parameters [19-21] or applying post-build heat treatments [17]. These advantages of the AM process indicate that it could potentially replace both the mechanical milling process and the consolidation process in the production of ODS alloys.

An optimized laser powder bed fusion (LPBF) process typically enhances strength while reducing work hardening and ductility due to the unique microstructure of fine grains and dislocation cells formed during rapid localized solidification [19,22-24]. Recent tests indicate that these fine-grained structures, along with mobile dislocations, can shorten high-temperature creep life [13,14,20]. Additionally, fracture toughness of AM materials may decrease due to increased porosity from the build process, structural anisotropy relative to the build direction, and inclusions from impurities in the feedstock powder [15,25]. Neutron or ion irradiation can also significantly impact behaviors observed in AM alloys, such as shortened creep life and reduced fracture toughness [15,26-28]. These degradation mechanisms may be more pronounced in ferritic alloys and ferritic–martensitic steels [29,30]. Given the combination of embrittling features from AM processing—high porosity, incomplete transformation, and a metastable state with high residual stress—manufacturing reactor components may necessitate a post-build process to achieve high-performance alloys, often involving controlled thermomechanical processing (TMP). Therefore, the production of AM-based components requires a processing route that integrates multiple materials processing methods, which is pursued in this research.

To expedite the development of ODS alloys, this research explores novel manufacturing routes combining AM methods with traditional thermomechanical processing [31-35]. Specifically, a LPBF process and post-build hot-rolling treatments were integrated into the production of ODS austenitic alloys, such as Fe-Cr-Ni alloys like 316L and 316H. The study conducted comprehensive microstructural and mechanical characterizations to assess the performance of the newly developed materials and provide insights for future process design. This report outlines the processing routes for ODS alloys that combine AM processes with post-build thermomechanical treatments and details the mechanical and microstructural characteristics of the AM ODS alloys.

2. Materials Processing and Characterization

This research aims to demonstrate the feasibility of AM technology in conjunction with traditional processing methods for producing ODS alloys. Commercial 316L and 316H powders were chosen for this demonstration, and key mechanical properties — including uniaxial tensile testing and fracture toughness testing — were conducted to verify their characteristics. Microstructural examinations were also performed to correlate with the mechanical performance of the newly produced ODS alloys. Experimental procedures are detailed in the following sections.

2.1 Processing for AM ODS Alloys

Two austenitic alloy powders, 316L (low carbon) and 316H (high carbon) powders, served as the base materials for producing ODS alloys. These powders, with nominal chemistries falling within standard composition (in wt.%) ranges (Fe-17Cr-12Ni-2.5Mo-0.03C for 316L and Fe-17Cr-12Ni-2.5Mo-0.07C for 316H), were both produced via argon gas atomization by Praxair, with a powder particle diameter ranging from 15 to 45 µm. In the AM process, the yttria (Y_2O_3) powder from ThermoFisher Scientific Chemicals, with an average particle size of less than 50 nm and a high purity of 99.995%, was added to the alloy powders and thoroughly mixed to introduce oxygen content and/or nano-oxide particles. Traditionally, the optimal or typical amount of yttria powder added to a base alloy is approximately 0.3 wt.% [5-11]. Due to the rapid and possibly localized formation of nanoparticles, part of the oxygen source is expected to be not effectively used during AM process, leading to a highly uneven oxygen distribution afterward. To compensate for this loss and to ensure sufficient microstructural integrity, an amount higher than the optimal content—0.5 wt.%—was added to both austenitic alloys. Excessive oxygen content is expected to reduce ductility, as oxide particles or clusters are considered the primary crack initiation sites in AM alloys [33]. We assume that the high ductility inherent in the austenitic stainless-steel matrix allows the AM ODS alloys to accommodate this increased oxide content (by 0.2%) while retaining sufficient ductility (i.e., avoiding embrittlement) for structural applications.

The LPBF method was used to consolidate mixtures of austenitic alloy powders with oxide powders. Rotary mixing was performed for 2 hours in a drum blender at approximately 20 rpm. The SS316L +

yttria and SS316H + yttria powder blends were then processed using a Renishaw AM250 LPBF system. This system features a 400 W ytterbium-fiber pulsed laser with a spot size of approximately 70 µm and a wavelength of 1.07 µm. Six plates, each measuring 62 mm wide, 37 mm high, and 12 mm thick, were printed for the two powder mixtures using the following parameters: laser power set at 225 W, point distance of 65 µm, exposure time of 105 µs, hatch spacing of 100 µm, and a layer thickness of 50 µm. A standard stripe pattern linear hatch scan strategy was employed, with a stripe width of 5 mm and a scan rotation of 67° between consecutive layers. All printing operations were conducted at room temperature within an inert argon atmosphere, maintaining oxygen levels below 500 ppm, and using a mild steel build plate. Subsequently, these plates were sectioned into bars measuring 14–17 mm in height for ease of subsequent thermomechanical processing.

Table 1. Materials and processing of AM austenitic ODS alloys

Material ID	Base Alloy Composition	AM method	TMP condition
AM ODS 316L	316L	LPBF	None
AM ODS 316L-700°C	316L	LPBF	Hot-rolling at 700°C for 70% reduction
AM ODS 316L-800°C	316L	LPBF	Hot-rolling at 800°C for 70% reduction
AM ODS 316H	316H	LPBF	None
AM ODS 316H-700°C	316H	LPBF	Hot-rolling at 700°C for 70% reduction
AM ODS 316H-800°C	316H	LPBF	Hot-rolling at 800°C for 70% reduction

The second or final step of the production process involved controlled hot-rolling processes: the bars underwent thermomechanical processing through repeated processes of hot-rolling and annealing at either 700°C or 800°C for 10 minutes. This rolling process included multiple (5 to 6) annealing–rolling cycles, ultimately reducing the thickness of the rolled coupons to approximately 5 mm. This height reduction corresponds to a plastic strain of approximately 70%. In total, six different materials were produced, consisting of two alloys under three different TMP conditions, as summarized in Table 1.

2.2 Mechanical property evaluation of AM ODS alloys

From the hot-rolled coupons, two types of testing specimens were machined for mechanical property evaluations: miniature tensile specimens and fracture specimens, shown in Figures 1(a) and 1(b), respectively. The face-normal direction of these specimens coincides with the build direction in the AM process, which also corresponds to the direction of thickness reduction during hot-rolling. The first type of specimen is the SS-J2 tensile specimen, featuring a gauge section that is 1.2 mm wide, 0.5 mm thick, and 5 mm long. The total length of the specimen is 16 mm, with a head width of 4 mm. The second type is a miniature bend-bar specimen (MBS) with side grooves, intended for pre-cracking and static fracture testing under three-point bend (TPB) loading mode. This specimen is rectangular, measuring 14 mm in length, 4 mm in width, and 2.5 mm in thickness. At the midpoint of the bar, a 1-mm deep electrical discharge machined notch was introduced, and 20%-deep grooves were machined on both sides of the specimen.

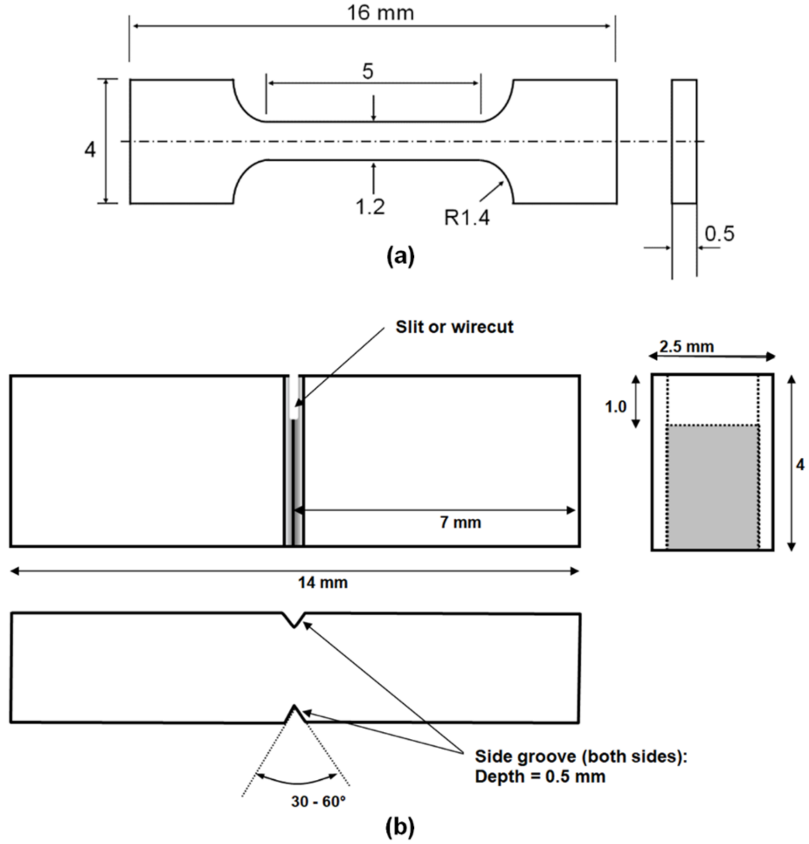

Figure 1. Miniature mechanical testing specimen designs: (a) SS-J2 tensile specimen and (b) three-point bend bar specimen.

Uniaxial tensile testing of SS-J2 specimens was conducted at room temperature, 300°C, and 600°C using an electromagnetic mechanical testing system, with a nominal strain rate of 1×10^{-3}/s (equivalent to a displacement rate of 0.3 mm/min), employing shoulder-loading grip sets [36]. The loading direction was aligned with either the rolling direction or laser scanning direction if not rolled. Raw data, specifically load-displacement data up to failure, were recorded and utilized to determine common engineering strength and ductility parameters, including yield strength (YS), ultimate tensile strength (UTS), uniform elongation (UE), and total elongation (TE). Unless otherwise specified, tensile testing and data analysis followed the standard procedures outlined in ASTM E8/E8M and ASTM E21.

Fracture toughness testing in TPB mode was also performed at room temperature, 300°C, and 600°C using the same mechanical testing system. The span of the TPB loading was 3 mm. A streamlined procedure from precracking to static fracture testing to fracture toughness calculation, which was established for miniature fracture testing by the lead author [6,5,37], was applied to the fracture toughness testing of the 14 mm long miniature specimens. The omission of the externally attached clip gage for displacement measurements and the use of the self-guiding, cradle-type specimen grip both enabled high-efficiency testing in this project. A simplified fracture resistance (J-integral) vs. crack growth resistance (J-R) curve calculation procedure was established by adopting the load-displacement curve normalization method in ASTM E1820 with a slight modification that separates the displacement measurements into elastic and plastic components. Before the static fracture (J-R) testing, every single-edged MBS specimen was fatigue-precracked in load range control mode to create a sharp crack tip extending from the 1 mm deep machined notch. The resulting sharp fatigue precrack (initial crack length for static fracture testing) tip was extended to an approximately 1.8 mm total depth, or ~45% of the specimen thickness. Creating a sharp crack in front of the notch tip is required to conduct a static fracture toughness test to evaluate fracture resistance and critical stress intensity (*K*) values.

The static fracture tests were conducted in TPB loading mode at a displacement speed of approximately 0.005 mm/s (0.3 mm/min). Monotonic load vs. displacement data were recorded at a typical data acquisition rate of 5 Hz during the static testing. These data were used to generate J-R curves and determine fracture toughness values (J_Q and K_{JQ}). The J-R curves were constructed from the load-displacement curve data and optical measurements of crack lengths using a modified curve normalization method tailored for miniature specimens. Aside from a few specialized techniques used for miniature specimens, the fracture testing and calculation practices adhered to ASTM Standard Test Methods E1820 and E399. The following special techniques were employed during the fracture testing and data analysis: (a) The fracture resistance (J-R) testing did not utilize any attached gauge for displacement measurement. To calculate the load-displacement curve, the linear displacement component—comprising pure elastic displacement and machine load-line compliance—was subtracted, and the elastic displacement was reconstructed using theoretical equations. (b) The ratio of final uncracked ligament length to initial ligament length was assumed to be proportional to the ratio of the end-of-test load to the maximum load, i.e., an effective final crack length was used in the calculations rather than the physical final crack length (c) Precracking was initiated based solely on the cyclic peak displacement reading. Fatigue crack length attainment was determined when the displacement peak changed by a defined amount under a given load amplitude.

The final step of the fracture data analysis involved determining the fracture toughness values according to ASTM E1820 standard. For each test, the interim fracture toughness (J_Q) in terms of energy (kJ/m² or kN/m) was determined from the J-R curve. The J_Q value was identified at the intersection of the J-R curve and the 0.2 mm offset line from the crack blunting line (the initial linear segment of the J-R curve). Subsequently, the J_Q values were converted to the fracture toughness values in terms of stress intensity (K_{JQ}) using the equation specified in the ASTM standard.

2.3 Microstructural characterization

Microstructural analysis of the newly developed ODS alloys was performed using two types of electron microscopes: a TESCAN MIRA3 scanning electron microscope (SEM) with an Oxford Instruments electron backscatter diffraction (EBSD) detector, and an FEI Talos 200 keV scanning transmission electron microscope (STEM). The STEM was equipped with a high-brightness X-field emission gun, bright-field (BF) and multiple annular dark field detectors, and a FEI ChemiSTEM energy dispersive X-ray spectroscopy (EDS) system for elemental analysis. Colored inverse pole figure (IPF) maps for grain structures were obtained from the SEM, while STEM-BF images revealing subgrain and dislocation structures, as well as STEM-EDS elemental maps showing nanoparticles and compositions, were captured using the STEM. All STEM sample preparation has been carried out in a FEI Versa 3D focused ion beam scanning electron microscopy (FIB-SEM). It should be noted that the microstructural characterization was conducted on the AM ODS 316L and 316H alloys in the as-built and 700°C hot-rolled conditions. This was because the microstructures of the alloys in the 800°C hot-rolled condition were expected to be similar to or slightly coarser than those of the 700°C hot-rolled alloys.

3. Mechanical Test Results

The test results for the newly produced AM austenitic ODS alloys are summarized in the following subsections. The temperature dependencies of engineering strength (YS and UTS) and ductility (UE and

TE) are presented and compared among the six different processing routes. Fracture toughness data for the ODS alloys are also included. These comparisons may guide the selection of a more feasible alloy and processing route among the ODS materials.

3.1 Stress-strain behavior and temperature dependence of strength and ductility

Figure 2 illustrates the stress-strain curves of six AM ODS alloys obtained from tensile tests conducted at various temperatures. At room temperature (RT) and 300°C, the curves consistently show that the as-built alloys have the lowest flow stresses and highest elongations among the datasets, while the alloys hot-rolled at 700°C exhibit the highest flow stresses and the alloys treated at 800°C demonstrate intermediate strength and ductility levels. Regarding elongation, an inverse relationship is observed: the as-built alloys display the highest elongation, whereas the alloys treated at 700°C show the lowest elongation. However, the tensile stress-strain behavior at 600°C deviates from the trends observed at RT and 300°C. In general, the as-built alloys still exhibit lower strength and higher elongation compared to the hot-rolled processed alloys, which now demonstrate similar strength and elongation characteristics overall. Overall, the data indicates a consistent trend of decreasing strength with increasing tensile test temperature. It is also noteworthy that dynamic strain aging, indicated by the serrated stress-strain curves, is observed in the as-built alloys tested at 600°C [38,39]. This phenomenon significantly reduces ductility at this high test temperature, as evidenced by the temperature dependence of tensile ductility parameters.

The tensile properties of austenitic ODS 316L and 316H alloys under six different conditions, which were determined using the stress-strain curves in Figure 2, are summarized in Figures 3 and 4. These figures depict their strength and ductility values as functions of test temperature. First of all, their room temperature (RT) strengths are impressively high, demonstrating 200–350% of those of wrought (annealed) 316-series stainless steels. Note that the wrought 316L and 316H steels in an annealed condition typically exhibit yield strength (YS) and ultimate tensile strength (UTS) values of about 250 MPa and 550 MPa, respectively [15]. When applying a YS criterion of 800 MPa for classification as an ODS alloy, typical for ferritic ODS alloys, only the AM ODS 316L-700°C material meets this criterion. The AM ODS 316H-700°C and AM ODS 316L-800°C materials almost meet the criterion. Meanwhile, the as-built ODS materials, namely AM ODS 316L and AM ODS 316H, also exhibit significantly higher strengths compared to their wrought counterparts. If compared among AM materials, however, their strengths are only marginally (20–30%) higher than those of AM 316L without oxide strengthening [15].

The temperature dependence of strength parameters is monotonic for all six AM ODS alloys. In Figure 3(a), the temperature dependencies of YS in six different alloy and microstructure conditions are compared. It is observed that YS decreases monotonically with test temperature from room temperature (RT) to 600°C, and both 316L and 316H materials exhibit similar temperature dependencies. The as-built ODS 316L and 316H alloys exhibit the lowest YS values among the six materials, while the 700°C treated ODS 316L alloy demonstrates the highest strength across all test temperatures. Application of a multistep hot-rolling process increased the strength of AM 316LSS at all test temperatures, with the 700°C TMP (~70% total strain) resulting in higher strength gains compared to the 800°C TMP. Figure 3(b) compares the ultimate tensile strength (UTS) data of AM ODS 316L and 316H stainless steels in three different conditions. High UTS values (650–950 MPa) are measured for all 316 alloy variants at room temperature (RT), with values decreasing with increasing test temperature. Additionally, the strength dependence in the six AM ODS 316L and 316H materials shows a monotonic decrease, with strengths decreasing by 30–40% as temperature increases from RT to 600°C. Another important observation is the relatively low work hardening capacity between the initial yielding and the initiation of plastic instability or necking compared to wrought alloys. For these austenitic ODS materials, their UTS values are approximately 12% higher than the corresponding YS values, whereas wrought materials typically exhibit some 20–30% increases between YS and UTS. This difference may be attributed to the high-energy and high-strength microstructures of AM ODS 316L and 316H alloys, where the high-density defect levels restrict further accumulation of defects and thus deformation hardening before encountering instability in deformation uniformity.

Figures 4(a) and 4(b) compare the uniform elongation (UE) and total elongation (TE) data of the AM austenitic ODS alloys. At room temperature, the ODS 316L in the as-built condition exhibits the highest ductility among the tested materials, with UE at approximately 20% and TE exceeding 25%. Following closely, the ODS 316H in the as-built condition shows the next highest ductility. Meanwhile, the AM ODS alloys subjected to 700°C and 800°C TMPs demonstrate relatively lower ductilities compared to the as-built conditions, attributed to the significant increase in strength from the TMPs. Despite this, the ductility of the AM austenitic ODS alloys remains significant (all TEs > 4%), with no embrittlement observed across the tested alloys and TMP conditions. However, it is notably lower than the high ductility (often >50% TE) typically observed in wrought 316-series stainless steels. Another notable aspect observed is the necking ductility (TE-UE). Significant necking ductility is crucial as it helps prevent catastrophic crack growth in structures under load. The necking ductility value (TE-UE) is approximately proportional to the uniform elongation (UE) and total elongation (TE) of the alloy. Measurements for the AM ODS steels fall within a relatively narrow range of 2.5–9.5%, which is similar to the TE-UE data measured for the AM and wrought (non-ODS version) 316L alloy [15].

Both uniform elongation (UE) and total elongation (TE) values exhibit a rapid decrease with test temperature below 300°C, with their temperature dependence becoming less pronounced in the higher temperature range of 300–600°C. Over this elevated-to-high temperature range, the temperature dependencies of these ductility parameters are milder compared to those of yield and ultimate tensile strengths, albeit relatively smaller and more variable. In general, the AM ODS 316 materials with higher tensile strength demonstrate lower ductility, which aligns with observations in many metallic materials. Specifically, lower ductilities are measured for the higher tensile strength AM ODS 316L and 316H alloys treated at 700°C. Additionally, a ductility minimum is observed either at 300°C or 600°C, with a tendency for alloys with relatively higher ductility to exhibit a minimum at 300°C, while higher tensile strength materials show a minimum at 600°C. This reduced ductility at specific temperatures is likely influenced by the dynamic strain aging effect [38,39].

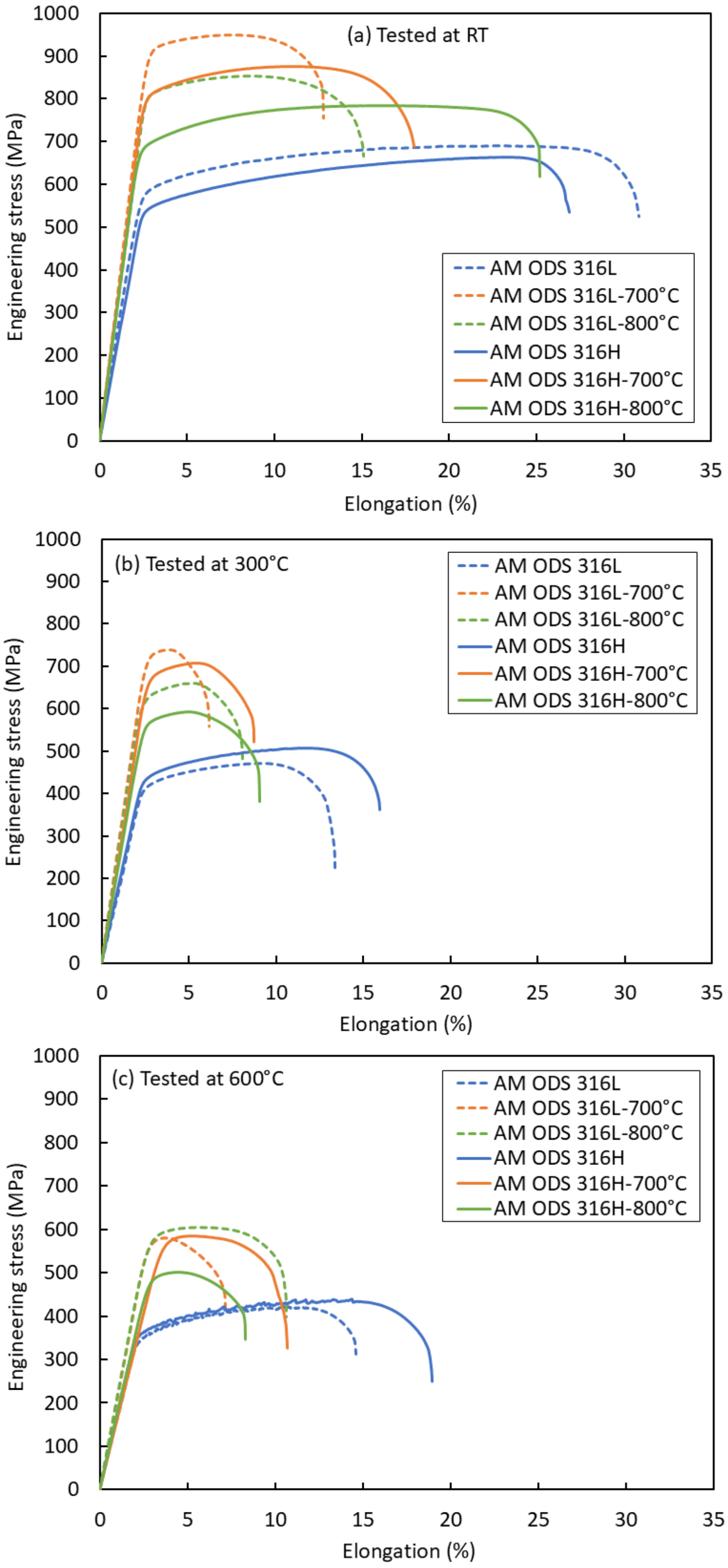

Figure 2. Engineering stress-strain (elongation) curves of the AM ODS 316L and 316H alloys at (a) RT, (b) 300°C, and (c) 600°C

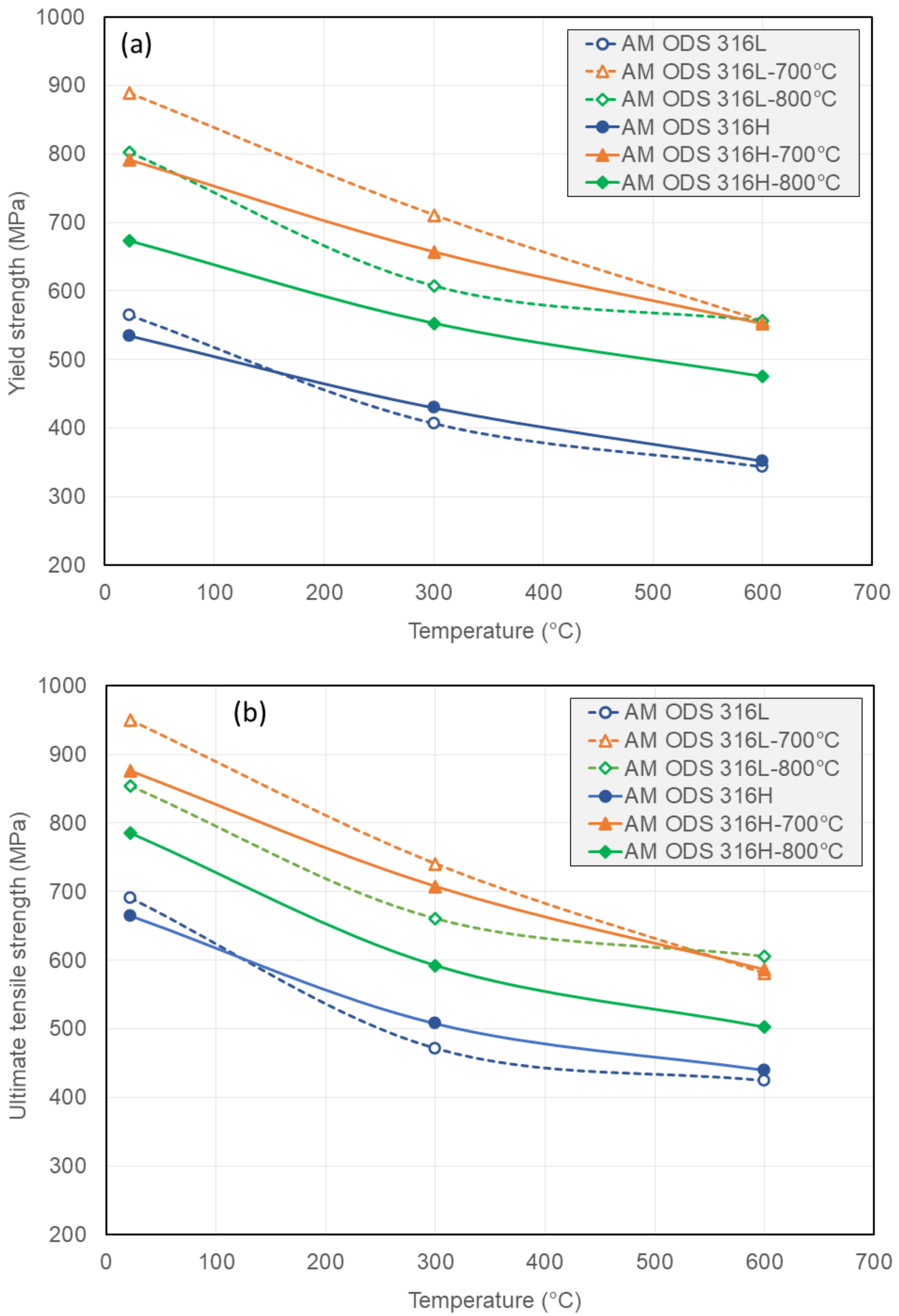

Figure 3. Temperature dependence of tensile strength for AM ODS alloys with and without post-build TMP: (a) yield strength and (b) ultimate tensile strength

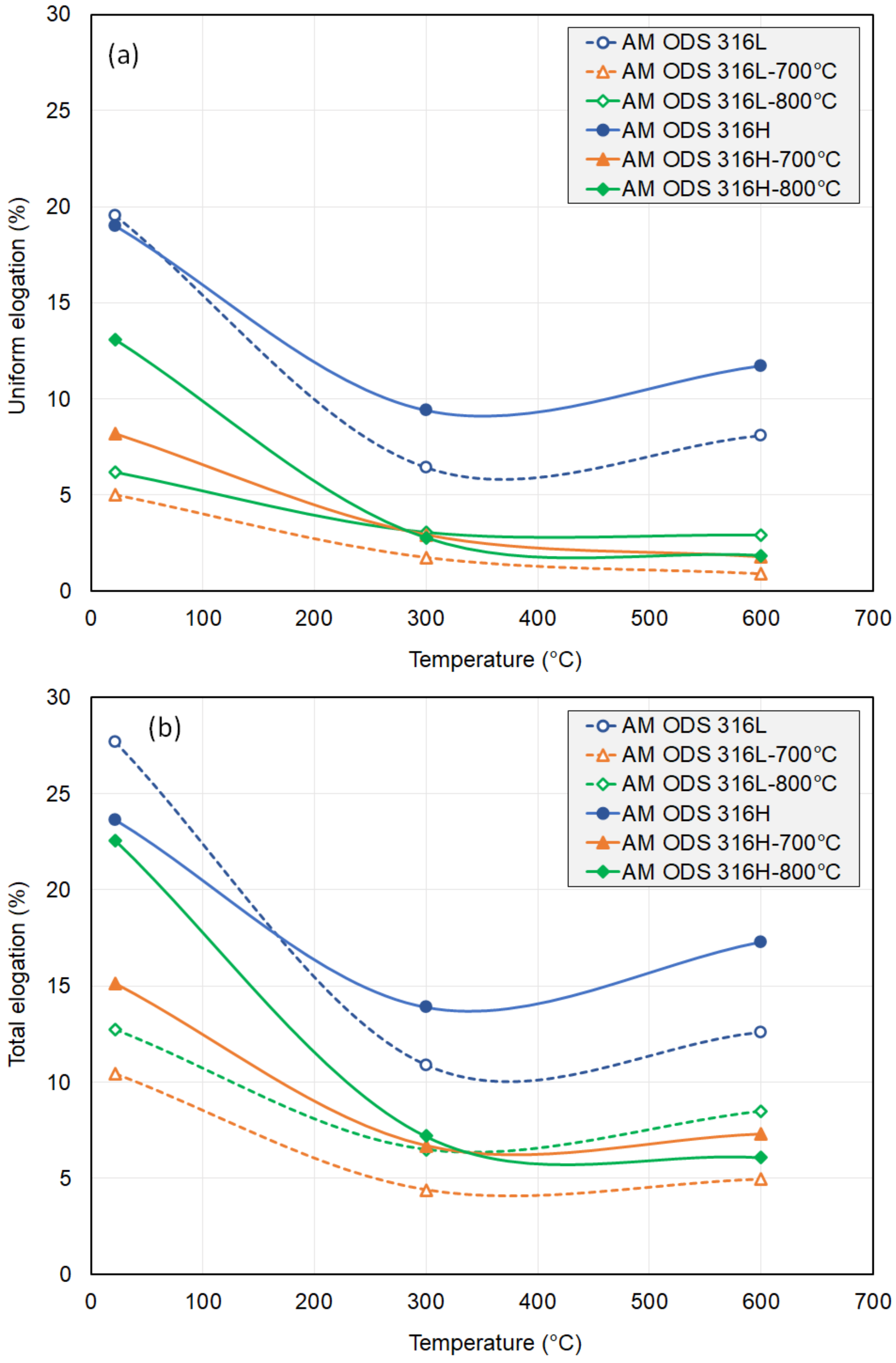

Figure 4. Temperature dependence of tensile ductility for AM ODS alloys with and without post-build TMP: (a) uniform elongation and (b) total elongation

3.2 Temperature dependence of fracture resistance behavior

The fracture resistance curves (J-integral value versus crack extension curves) for the six AM ODS alloys are depicted in Figure 5. As detailed in section 2.2 for data processing, each fracture toughness (J_Q) value was determined from the J-R curve at the intersection point with the 0.2 mm offset line of its initial linear segment. It is noteworthy that the fracture toughness parameter (K_{JQ}) data represents the resistance to initial crack growth, whereas the J-R curves illustrate the overall resistance of the alloy to crack extension, encompassing both maximum stable crack growth ability and the sustainability of high tearing modulus (or slope of the J-R curve). Below, both the J-R curves and K_{JQ} data are presented and discussed to compare the effects of processing routes and test temperatures on the fracture performance of AM ODS alloys.

In the J-R plots in Figure 5, the as-built samples consistently exhibit higher J-integral values compared to the samples treated with hot rolling deformation, regardless of test temperature. This indicates that the as-built alloys generally possess greater overall fracture resistance than the treated samples, which show lower J-integral values. Specifically, the as-built alloys demonstrate higher initial J-integral values, which correlate with higher fracture toughness (J_Q) values, as well as a steeper increase in J-integral values with crack extension ($\Delta J/\Delta a$). This latter resistance behavior is crucial for providing sustained cracking resistance in structural applications. The superior fracture resistance of the as-built ODS alloys may be attributed to an optimal combination of strength and ductility, as detailed in Section 3.1. For instance, the yield strengths of the 700°C hot-rolled ODS alloys are 50–70% higher than those of the as-built ODS alloys, but their elongations are significantly lower, only a small fraction of those observed in the as-built alloys. Thus, the reduction in toughness due to decreased ductility from post-built treatments outweighed the corresponding gains from strengthening effects.

While the decrease in fracture resistance (J-R) after post-built treatment was significant, the distinction between the effects of 700°C and 800°C treatments was minimal, although the higher temperature treatment tended to retain slightly higher cracking resistance. It was also observed that increasing the test temperature led to a decrease in J-integral values across all samples, though the decrease between 300°C and 600°C was smaller than that between 25°C and 300°C. This decline with rising temperature suggests reduced crack propagation resistance as temperature increases. Nevertheless, despite these variations, all 18 fracture tests conducted in the research exhibited stable cracking processes, indicating no discernible differences in fracture modes among the different alloys and post-build treatments.

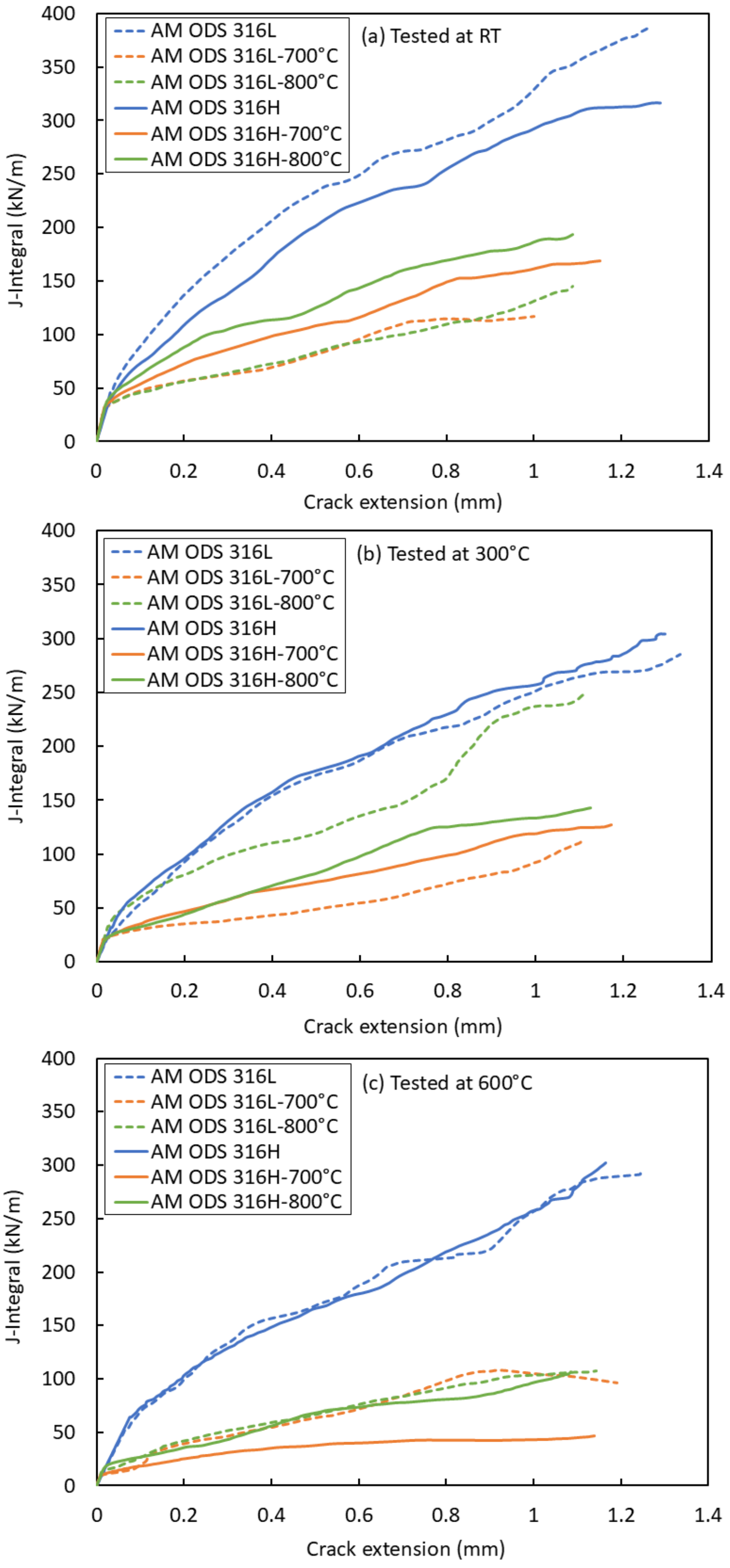

Figure 5. Fracture resistance (J-R) curves of the AM ODS 316L and 316H alloys at (a) RT, (b) 300°C, and (c) 600°C

Figure 6 illustrates the temperature-dependent fracture toughness (K_{JQ}) of AM austenitic ODS materials. As discussed in the section on J-R curves, both the 316L and 316H alloys in their as-printed condition demonstrate robust fracture toughness values exceeding 150 MPa√m across the entire temperature range tested, although showing significant temperature dependence. In contrast, all other materials subjected to post-build TMPs exhibit considerably lower fracture toughness, ranging narrowly from 110 to 150 MPa√m at RT, with a steady decrease as the test temperature rises. Importantly, all fracture toughness values fell below 100 MPa√m at 600°C, indicating insufficient fracture toughness for applications in very high stress and temperature environments. Furthermore, these fracture toughness versus temperature curves, which show a monotonic decrease with temperature, suggest that room temperature falls within or near the upper shelf of the materials' temperature transition curve. The temperature dependencies across the six alloys are relatively consistent, suggesting that increasing application temperature may not enhance fracture performance of these materials, thus favoring lower temperature applications. Despite these limitations, the application of austenitic ODS alloys processed via AM and post-build TMPs may offer greater feasibility across a broader range of conditions compared to general ferritic ODS materials [5]. The post-build process needs to be improved for these AM ODS alloys.

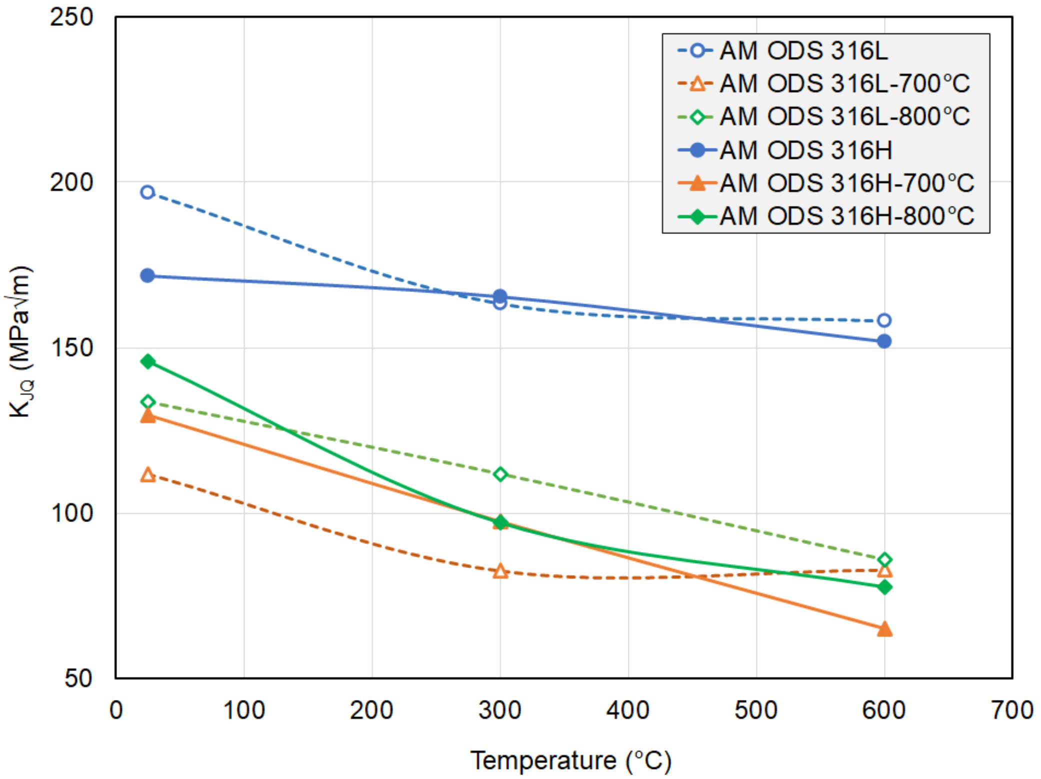

Figure 6. Temperature dependence of fracture toughness (K_{JQ}) for AM ODS alloys with and without post-build TMP

4. Discussion

Comparison of the mechanical properties in the above sections indicates that AM ODS 316L and 316H alloys can exhibit a wide range of mechanical performance, depending on the application of post-build

TMP. It is demonstrated that a reasonable balance of strength and ductility can be achieved without any post-build treatment. Moreover, employing a multistep TMP at 700°C can result in extremely high strength approaching 1 GPa, albeit with low ductility of only a few percent elongation. Additionally, it is observed that the fracture toughness of these alloys correlates closely with ductility, showing an inverse relationship with strength. Given that the LPBF process has been optimized and thus ensures consistent as-built properties without significant variations, it suggests that post-build TMP may be the critical factor leading to substantial changes. This section aims to elucidate the effects of post-build TMP on the microstructural and mechanical properties of the alloys, providing insights to guide further development of ODS austenitic alloys.

4.1 Effects of post-build processing on microstructure and mechanical performance

The SEM-EBSD images (IPF maps) of the four AM ODS 316L and 316H alloys are presented in Figure 7. The EBSD images depict fine grain structures in the as-built conditions (left column images) and significantly finer grain structures after hot-rolling at 700°C (right column images). The IPF maps of the two as-printed ODS alloys exhibit strong grain textures with a predominant orientation of [101] and large grain conglomerations containing subgrains with similar orientations, which are typical characteristics of AM materials [15,31-35]. These as-printed alloy images reveal many fine grains ranging from a few to tens of micrometers, with some grains being relatively larger, up to hundreds of micrometers. The average grain sizes are approximately 16 and 13 μm for the as-built 316L and 316H ODS alloys, respectively, which decrease to about 7 and 9 micrometers after the 700°C hot-rolling treatment. Furthermore, the textures become notably more uniform after hot rolling, with a significant increase in the population of grains oriented along [001]. Color variation within the same grain or subgrain is common across many grains, indicating pronounced crystal distortion due to high-density dislocations and residual stresses within the microstructures. In summary, the major effects of TMPs in these EBSD grain structures include grain refinement, enhanced uniformity in grain orientation, and high residual stress due to presence of high-density dislocations. Note that, due to the presence of grains with similar orientations and the resolution limitations of EBSD imaging, some grain boundaries are not clearly defined. The actual nanograin features of these ODS alloys require higher-resolution TEM or STEM imaging for further elucidation.

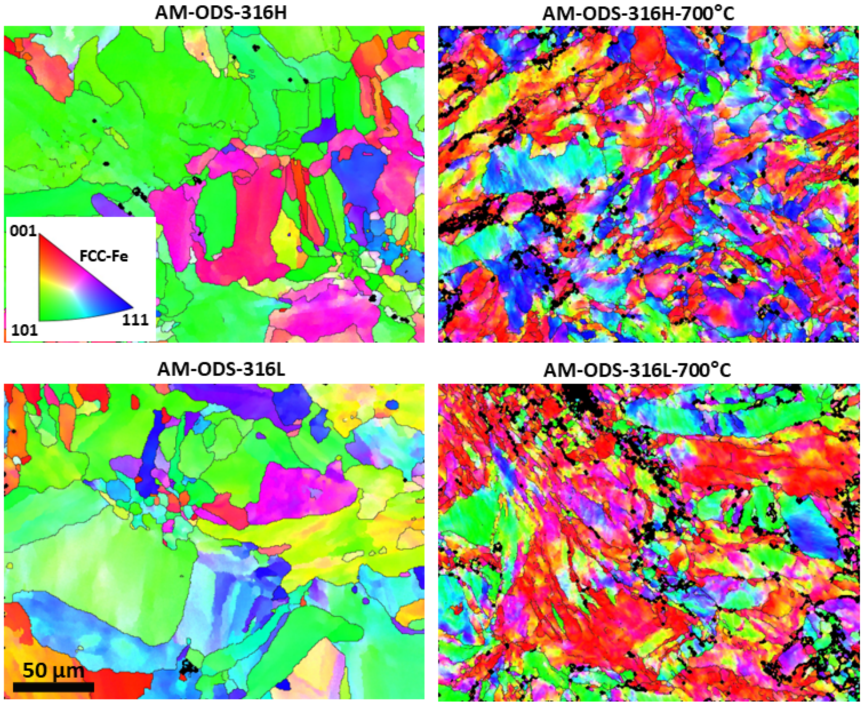

Figure 7. Grain structures of AM ODS 316L and 316H alloys in as-built and 700°C processed conditions (each image width is equivalent to 300 μm)

The first row of images in Figure 8 compares STEM-BF images of four AM ODS alloys, illustrating different nanostructures in both as-built and 700°C hot-rolled conditions. In the as-built ODS 316L and 316H alloys, the elongated subgrain structures and dislocation features are evident and are closely related to the melting pool formation and solidification behavior during LPBF process [15,34]. Following hot rolling, their microstructures exhibit increased deformation features, such as high-density dislocations and fragmented subgrain structures. The BF images indicate that the average subgrain width is approximately 600 nm before the 700°C hot rolling, and the microstructures become significantly narrower and more fragmented along the grain-elongation (hot-rolling) direction. In Figure 8, the elemental maps for Fe and Cr reveal distinct boundaries of subgrain structures produced by the AM process: Fe shows slight depletion while Cr is enriched in these boundary bands. Although these discernible bands persist in the hot-rolled condition, their intensity becomes fainter and more fragmented.

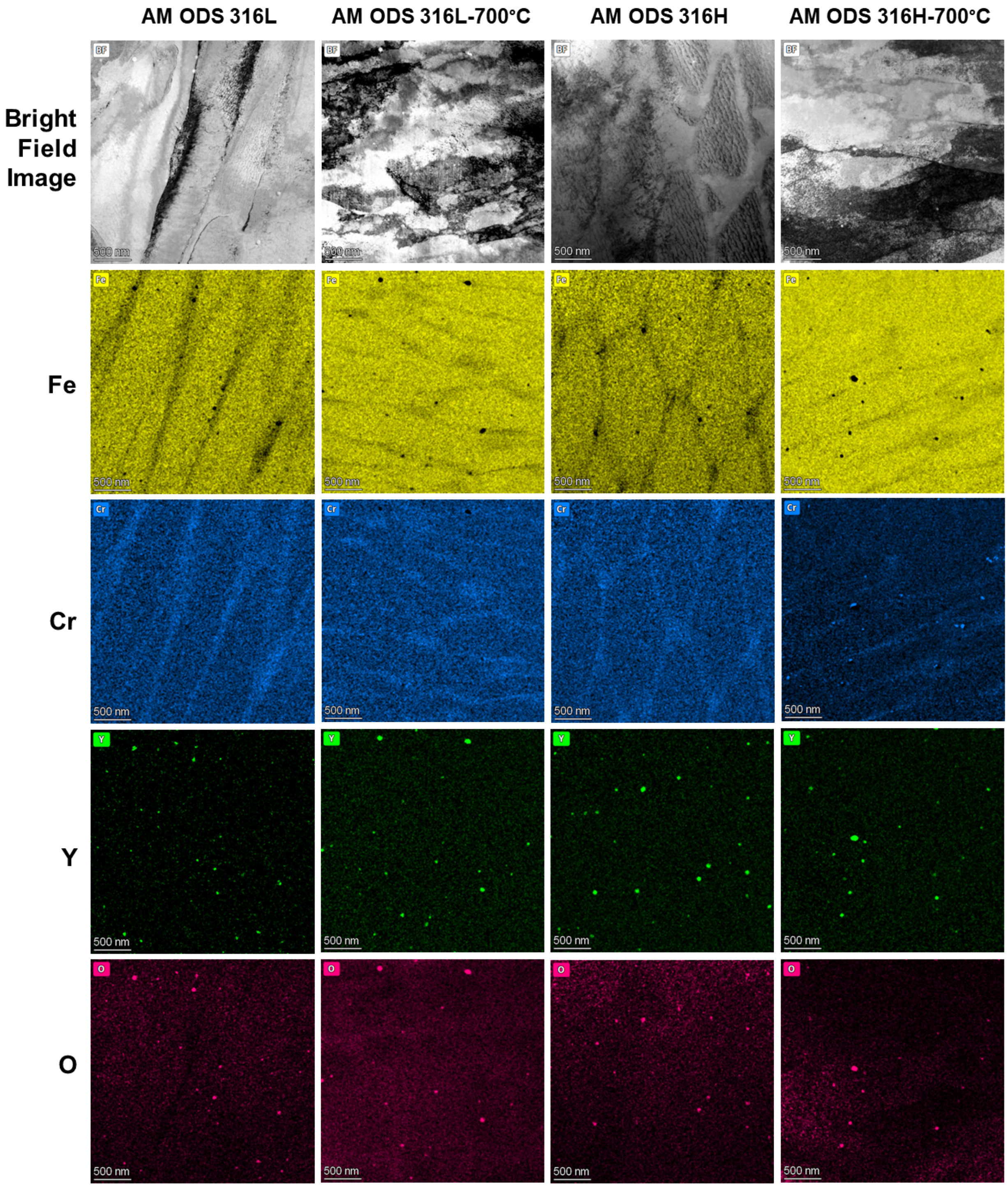

Figure 8. STEM-BF images and STEM-EDS elemental maps of AM ODS 316L and 316H alloys in as-built and 700°C processed conditions (each image width is equivalent to 3 μm)

The fourth and fifth rows in Figure 8 display elemental maps for Y and O, highlighting the distribution of yttrium oxide (Y_2O_3) or Y-O enriched nanoparticles. Comparison of these maps reveals several unique characteristics of particle distribution in AM austenitic stainless steels. According to Table 2, particle distribution statistics indicate that average oxide particle sizes fall within a narrow range of 26–32 nm, with significant deviations within each alloy and minimal differences observed among the four alloys. These particle sizes, though in the nanometer range, are relatively coarser compared to those typically found in ferritic ODS alloys (typically 2–5 nm) [5,6,9,32,40,41]. This disparity also confirms that finer oxide nanoparticles are less stable in close-packed austenitic (FCC structured) alloys than in ferritic (BCC structured) alloys. Consequently, the coarser particle distribution results in lower number densities in these austenitic AM alloys, ranging narrowly from 2.6–4.1×10^{19} particles/m^3.

Table 2. Summary of statistics for microstructural parameters

Materials:	AM ODS 316L		AM ODS 316L-700°C		AM ODS 316H		AM ODS 316H-700°C	
Microstructure Parameter	Average	Stand. Dev.	Average	Stand. Dev.	Average	Stand. Dev.	Average	Stand. Dev.
Grain Size (μm)	15.5	16.9	6.7	12.5	13.3	14.9	8.1	11.4
Y-O Rich Particle Density (m^{-3})	4.0E+19	8.0E+18	3.0E+19	6.0E+18	4.1E+19	8.2E+18	2.6E+19	5.1E+18
Y-O Rich Particle Diameter (nm)	26.9	8.5	28.9	14.2	29.2	11.8	31.6	13.1
Cr-O Rich Particle Density (m^{-3})							2.7E+19	5.3E+18
Cr-O Rich Particle Diameter (nm)							25.2	8.1

Comparison of particle size distributions also suggests that higher carbon content in 316H and post-build thermomechanical processing have not significantly influenced oxide particle formation during AM and subsequent processes (Figure 8 and Table 2). Specifically, the high-temperature severe plastic deformation at 700°C did not activate further processes affecting oxide particles, indicating insufficient thermal-mechanical activation at these temperatures to break down the existing particles formed during the AM process. Contrary to the Fe depletion and Cr enrichment at subgrain boundaries, oxide particles do not preferentially form along these boundaries, suggesting their formation likely occurred during earlier stages (at higher temperatures) of solidification. Interestingly, carbide (Cr-C rich or chromium carbide) particles are notably present in the higher carbon alloy AM ODS 316H-700°C only. In contrast, significantly fewer carbide particles are observed in the low carbon alloy (316L with < 0.3 wt.% carbon), resulting in negligible statistical data. The sizes and number density of these carbide particles generally fall at the lower end of the statistics observed for oxide particles. These observations indicate that these carbide particles were not produced during the AM process, which involves local melting and rapid cooling. Instead, the subsequent hot-rolling process at 700°C likely facilitated the formation of the carbides.

Comparing the mechanical properties after the post-build TMPs (Figures 2-5), the major microstructural effects that might have affected mechanical properties include grain refinement, formation of nanoparticles, and high-density dislocations. The AM ODS materials are renowned for their exceptional mechanical properties, leveraging, in particular, their fine grain structures, as revealed by EBSD maps. These materials exhibit high dislocation densities, possibly contributing significantly to their enhanced strength. Strengthening models for ODS steels state that the strength augmentation stems from the dual mechanisms of refined grain boundaries and a surplus of residual dislocations, both of which impede dislocation movement and thus increase strain hardening [1]. Evaluating the strengthening contributions of the grain refinements using the typical inverse square-root law on grain size (i.e., the Hall-Petch effect [42,43]), increases in the grain boundary hardening due to the 700°C TMP are approximately 52% and 28%, respectively, for AM ODS 316L and 316H alloys. Calculating with room temperature YS measurements, the actual total strengthening amounts are 75% and 48%, respectively, for the two alloys. These indicate the minor 23% and 20% increases in YS were contributed by the other features such as dislocations and nanoparticles formed during TMP, confirming that grain refinement is the major strengthening mechanism in the post-build processing. In fact, an optimized mechanical performance might require a critical balance: while strength typically increases with finer grains and higher dislocation densities, there is a trade-off with ductility. That is, overly refined microstructures and excessively dense dislocation networks can lead to diminished ductility due to increased fracture susceptibility and limited dislocation mobility. In addition, enhancing the precipitation of oxides and carbides is necessary to achieve higher densities and more optimized mechanical properties. Optimizing these parameters is crucial for tailoring AM ODS materials for specific applications that require a delicate balance between strength and ductility. Therefore, more effort is needed to optimize the processing steps to refine the microstructural components, particularly the distributions of grain sizes, nanoprecipitates, and dislocations.

Finally, the 316H alloy, with a higher carbon content (typically within 0.04–0.1 wt.%), shows lower or similar strength compared to 316L, which contains a limited amount of carbon (<0.03 wt.%), across all processing conditions. This relatively small or intermediate difference in strength might not significantly impact other mechanical properties. It is, however, notable that higher carbon content in ODS 316H alloy results in relatively lower strength. This might be related to the role of carbon as an austenite phase stabilizer, which can suppress the formation of ferrite phase during solidification and lead to the formation of larger austenite grains, resulting in lower strength and higher ductility. This warrants further investigation into the role of carbon content in strengthening mechanism of AM materials.

4.2 Inverse relationship between strength and fracture toughness and performance limitation

The mechanical performance of structural alloys is assessed using key property parameters such as strength, ductility, fracture toughness, creep rate, and fatigue limit, depending on their application environment. Optimizing manufacturing process and thus improving alloy performance can leverage this inverse relationship, for which enhancing both parameters is essential without sacrificing one for the other. These properties often exhibit a dependent or independent relationship with each other. It is well-established that strength and ductility frequently have an inverse relationship [44,45], as discussed in Section 3.2. Another critical correlation used to evaluate performance improvement involves fracture toughness and strength [44,46]. Generally, the fracture toughness of an alloy can decrease due to strengthening mechanisms like cold work, precipitation, and irradiation. Therefore, an inverse proportionality between fracture toughness and strength is commonly observed in many alloy groups [44, 46-48]. In Figure 9, fracture toughness data are plotted against corresponding yield stress data to identify general or unique behaviors at each test temperature. These plots consistently confirm the inverse relationship between strength and fracture toughness across different test temperatures. This relationship is expected to hold, provided that the processing route for the alloy does not significantly alter fundamental characteristics such as grain boundary bonding, alloy composition, constituent phases, and stacking fault energy [44]. Any substantial changes in these factors can fundamentally affect deformation and fracture behaviors in alloys.

Based on the mechanical behaviors detailed in Section 3, it is believed that the mechanical deformation and failure mechanisms remain consistent for the current AM ODS alloys despite differences in carbon content and processing routes. This implies that modifying these fundamental properties may be necessary to achieve genuine improvements in an alloy, resulting in fracture toughness data positioned higher and/or to the right relative to the current data. In Figure 9, no significant deviations from the trend curves are found at any temperature, indicating that all six materials are following the simple inverse relationship curves. Any changes in processing route and alloy composition in the current research have been improving one property but with sacrificing the other.

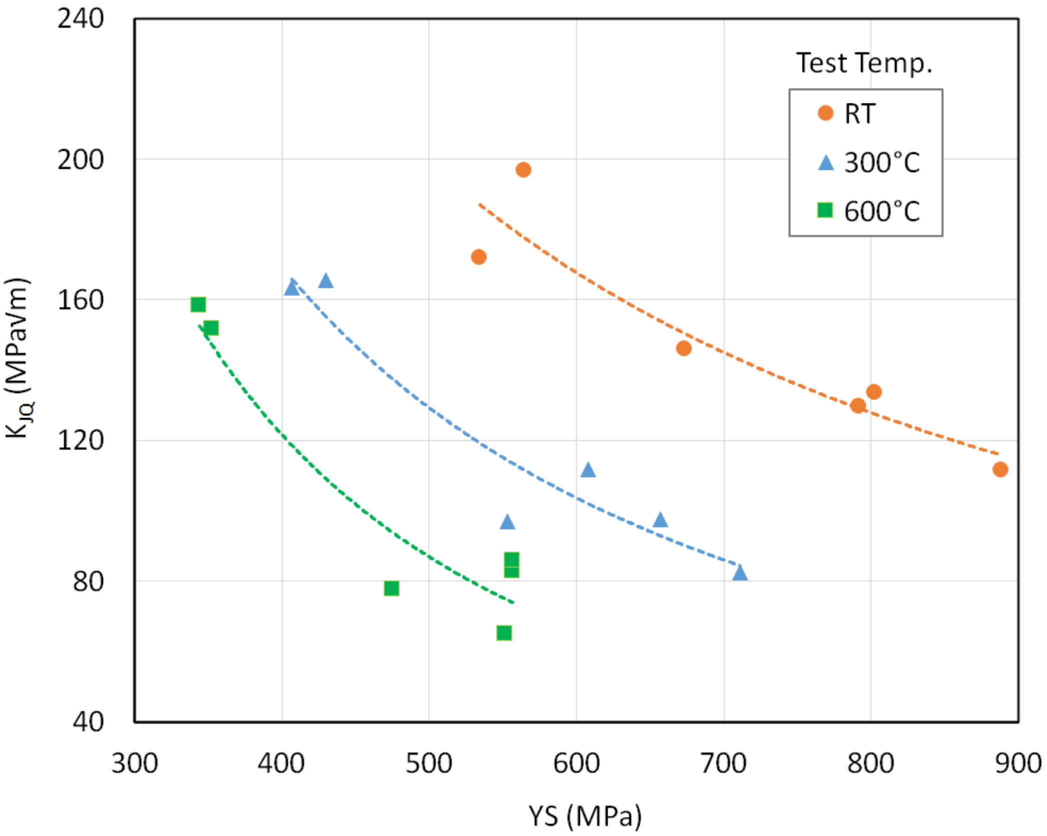

Figure 9. Inversely proportional relationship between yield strength and fracture toughness at three different test temperatures

5. Summary and Conclusions

This research aimed to explore an accelerated development path for ODS alloys by integrating AM technology with recent advancements in ODS materials and traditional steel processing. An AM and post-build processing route was devised for ODS austenitic alloys (i.e., AM ODS 316L and 316H), with detailed microstructural and mechanical characterizations providing insights into the alloy and processing concepts. New processing routes for ODS alloys combined mechanical mixing of alloy and oxide powders, LPBF processes, and post-build TMPs, including 700°C and 800°C controlled hot-rolling steps to apply severe plastic deformation (~70% strain) to the as-built materials. The following conclusions were drawn from the characterization and analysis of properties and microstructures:

[1] The room temperature strengths of AM ODS 316L and 316H materials were impressive, reaching approximately 890 MPa and 950 MPa respectively for the highest YS and UTS in AM ODS 316L after 700°C TMP, demonstrating overall 200–350% of those of annealed wrought 316-series stainless steels. The temperature-dependent strength of AM ODS alloys exhibits a consistent decrease in YS and UTS with increasing temperature up to 600°C, with the lowest strength observed in the as-built conditions and the highest in the 700°C treated ODS 316L alloy.

[2] The AM ODS 316L in its as-built state showed the highest ductility among the tested materials, with UE at approximately 20% and TE exceeding 25% at RT. The AM ODS 316H in the as-built condition

closely follows with the next highest ductility. However, the ductility of AM ODS alloys subjected to 700°C and 800°C TMPs decreased significantly due to the significant strength increase. Nonetheless, all AM austenitic ODS alloys maintain significant ductility (TEs > 4%), without exhibiting embrittlement across the tested alloys and TMP conditions.

[3] Both 316L and 316H alloys in their as-printed state demonstrate robust fracture toughness values exceeding 150 MPa√m across all tested temperatures, but post-build TMPs result in lower fracture toughness values ranging narrowly from 110 to 150 MPa√m at room temperature. This toughness declines steadily with increasing temperature, dropping below 100 MPa√m at 600°C, limiting their suitability for high-stress, high-temperature applications.

[4] SEM-EBSD images of AM ODS 316L and 316H alloys reveal finer grain structures post-700°C hot-rolling compared to their as-built states, with as-built conditions showing distinct grain textures dominated by [101] orientations and conglomerations of fine grains. Average grain sizes for both alloys decreased from 13-16 µm and to 7 - 9 µm after hot rolling. Thermal-mechanical treatment results in increased grain uniformity along [001] orientations, accompanied by visible crystal distortion due to residual stresses and high-density dislocations. These microstructural buildups—grain refinement and high dislocation density—are considered the main causes for the impressively high strength after TMPs.

[5] STEM-BF images highlight microstructural changes from elongated subgrains in as-built conditions to fragmented structures post-700°C hot-rolling, with STEM-EDS elemental maps indicating Fe depletion and Cr enrichment at subgrain boundaries. Particle distribution analysis shows Y-O rich nanoparticles averaging 26–32 nm, with lower number densities ($2.6–4.1\times10^{19}$ particles/m^3) in these austenitic AM alloys. Minimal impact from carbon content or TMP processes on oxide particle formation is observed, contrasting with the presence of chromium carbide particles in higher carbon 316H alloys after hot rolling.

[6] The YS and K_{JQ} of AM ODS alloys demonstrate a clear inverse relationship at each test temperature. Despite these alloys exhibiting impressive hardening capability with AM and TMP processes, essential for high-temperature applications, the strong inverse relationship suggests that efforts to enhance strength in these alloys must be balanced to prevent complete embrittlement. Overall, integrating AM technology with a tailored post-build processing route holds promise for advancing an economical ODS alloy development, despite the challenges in maintaining high fracture toughness at elevated temperatures.

6. Acknowledgement

This research was sponsored by the US Department of Energy Office of Nuclear Energy’s Advanced Materials and Manufacturing Technologies program and Office of Fusion Energy Sciences’ Foundational Fusion Technology Program under contract DE-AC05-00OR22725 with UT-Battelle LLC. The authors thank Dr. Weicheng Zhong and Dr. Tim Graening for their thoughtful review of this report before publication.

On behalf of all authors, the corresponding author states that there is no conflict of interest.

7. References

[1] Steven J. Zinkle, Jeremy T. Busby, "Structural materials for fission & fusion energy," *Materials Today,* 12 (2009) 12-19.

[2] Lizhen Tan, Thak Sang Byun, Yutai Katoh, Lance Lewis Snead, "Stability of MX-type strengthening nanoprecipitates in ferritic steels under thermal aging, stress and ion irradiation," *Acta Mater.,* 71 (2014) 11-19.

[3] M.B. Toloczko, D.S. Gelles, F.A. Garner, R.J. Kurtz, K. Abe, "Irradiation creep and swelling from 400 to 600 C of the oxide dispersion strengthened ferritic alloy MA957," *J. Nucl. Mater.,* 212 (1994) 604-607.

[4] Osman Anderoglu, Thak Sang Byun, Mychailo Toloczko, Stuart A Maloy, "Mechanical performance of ferritic martensitic steels for high dose applications in advanced nuclear reactors," *Metall. Mater. Transact.,* A44 (2013) 70-83.

[5] T.S. Byun, J.H. Kim, J.H. Yoon, D.T. Hoelzer, " High Temperature Fracture Characteristics of Nanostructured Ferritic Alloy (NFA)," *J. Nucl. Mater. ,* 407 (2010) 78-82.

[6] T.S. Byun, J.H. Yoon, S.H. Wee, D.T. Hoelzer, S.A. Maloy, "Fracture Behavior of 9Cr Nanostructured Ferritic Alloy with Improved Fracture Toughness," *J. Nucl. Mater.,* 449 (2014) 39-48.

[7] Thak Sang Byun, Ji Hyun Yoon, David T. Hoelzer, Yong Bok Lee, Suk Hoon Kang, Stuart A Maloy, "Process Development for 9Cr Nanostructured Ferritic Alloy (NFA) with High Fracture Toughness," *J. Nucl. Mater. ,* 449 (2014) 290-299.

[8] D.T. Hoelzer, "History and Outlook of ODS/NFA Ferritic Alloys for Nuclear Applications," *Trans. ANS,* 118 (2018) 1587-1590.

[9] D.T. Hoelzer, J. Bentley, M.A. Sokolov, M.K. Miller, G.R. Odette, M.J. Alinger, "Influence of particle dispersions on the high-temperature strength of ferritic alloys," *J. Nucl. Mater.,* 367–370 (2007) 166-172.

[10] X.L. Wang, C.T. Liu, U. Keiderling, A.D. Stoica, L. Yang, M.K. Miller, C.L. Fu, D. Ma, K. An, "Unusual thermal stability of nano-structured ferritic alloys," *J. Alloys & Compounds,* 529 (2012) 96-101.

[11] C.P. Massey, D.T. Hoelzer, P.D. Edmondson, A. Kini, B. Gault, K.A. Terrani, S.J. Zinkle, "Stability of a model Fe-14Cr nanostructured ferritic alloy after long-term thermal creep," *Scripta Mater.,* 170 (2019) 134-139.

[12] M.B. Toloczko, F.A. Garner, V.N. Voyevodin, V.V. Bryk, O.V. Borodin, V.V. Mel'nychenko, A.S. Kalchenko, "Ion-induced swelling of ODS ferritic alloy MA957 tubing to 500 dpa," *J. Nucl. Mater.,* 453 (2014) 323-333.

[13] K.G. Field, J. Simpson, M. N. Gussev, H. Wang, M. Li, X. Zhang, X. Chen, T. Koyanagi, K. Kane, A. Marquez Rossy, M. Balooch, and K.A. Terrani, "Handbook of Advanced Manufactured Material Properties from TCR Structure Builds at ORNL – FY19," ORNL/TM-2019/1328, Oak Ridge National Laboratory, 2019.

[14] T. S. Byun, M. N. Gussev, T. G. Lach, M. R. McAlister, J. J. Simpson, B. E. Garrison, Y. Yamamoto, C. B. Joslin, J. K. Carver, F. A. List, R. R. Dehoff, K. A. Terrani, M. Li, X. Zhang, "Mechanical Properties and Deformation Behavior of Additively Manufactured 316L Stainless Steel – FY 2020," ORNL/TM-2020/1574, Oak Rodge Nationalaboratory, 2020.

[15] T.S. Byun, B.E. Garrison, M.R. McAlister, X. Chen, M.N. Gussev, T.G. Lach, A. Le Coq, K. Linton, et al., "Mechanical behavior of additively manufactured and wrought 316L stainless steels before and after neutron irradiation," *J. Nucl. Mater.,* 548 (2021) 152849.

[16] B. M. Morrow, T. J. Lienert, C. M. Knapp, J. O. Sutton, M. J. Brand, R. M. Pacheco, V. Livescu, J. S. Carpenter, G. T. Gray, "Impact of Defects in Powder Feedstock Materials on Microstructure of 304L and 316L Stainless Steel Produced by Additive Manufacturing," *Metall. Mater. Trans. A,* 49 (2018) 3637–3650.

[17] T. Ronneberg, C. M. Davies, and P. A. Hooper, "Revealing Relationships between Porosity, Microstructure and Mechanical Properties of Laser Powder Bed Fusion 316L Stainless Steel through Heat Treatment," *Mater. Des.,* 189 (2020) 108481.

[18] A. J. Birnbaum, J. C. Steuben, E. J. Barrick, A. P. Iliopoulos, J. G. Michopoulos, "Intrinsic Strain Aging, Σ3 Boundaries, and Origins of Cellular Substructure in Additively Manufactured 316L," *Addit. Manuf.,* 29 (2019) 100784.

[19] U. S. Bertoli, B .E. MacDonald, J. M. Schoenung, "Stability of Cellular Microstructure in Laser Powder Bed Fusion of 316L Stainless Steel," *Mater. Sci. Eng. A,* 739 (2019) 109–117.

[20] M. Li, X. Zhang, W.Y. Chen, F. Heidet, T. S. Byun, K.A. Terrani, "Creep Behavior of 316L Stainless Steel Manufactured by Laser Powder Bed Fusion," *J. Nucl. Mater.,* 548 (2021) 152847.

[21] T. Kurzynowski, K. Gruber, W. Stopyra, B. Kuźnicka, E. Chlebus, "Correlation between Process Parameters, Microstructure and Properties of 316 L Stainless Steel Processed by Selective Laser Melting," *Mater. Sci. Eng. A,* 718 (2018) 64–73.

[22] C. R. Brinkman, "Elevated-Temperature Mechanical Properties of an Advanced Type 316 Stainless Steel, United States," ORNL/CP-101053, Oak Ridge National Laboratory, 1999.

[23] E. Garlea, H. Choo, C. C. Sluss, M. R. Koehler, R. L. Bridges, X. Xiao, Y. Ren, B. H. Jared, "Variation of Elastic Mechanical Properties with Texture, Porosity, and Defect Characteristics in Laser Powder Bed Fusion 316L Stainless Steel," *Mater. Sci. Eng. A,* 763 (2019) 138032.

[24] T. Pinomaa, M. Lindroos, M. Walbrühl, N. Provatas, A. Laukkanen, "The Significance of Spatial Length Scales and Solute Segregation in Strengthening Rapid Solidification Microstructures of 316L Stainless Steel," *Acta Mater.,* 184 (2020) 1–16.

[25] D. Kong, X. Ni, C. Dong, L. Zhang, C. Man, X. Cheng, and X. Li, "Anisotropy in the Microstructure and Mechanical Property for the Bulk and Porous 316L Stainless Steel Fabricated via Selective Laser Melting," *Mater. Lett. ,* 235 (2019) 1–5.

[26] J. Lin, F. Chen, X. Tang, J. Liu, S. Shen, and G. Ge, "Radiation-Induced Swelling and Hardening of 316L Stainless Steel Fabricated by Selected Laser Melting," *Vacuum,* 174 (2020) 109183.

[27] M. Song, M. Wang, X. Lou, R. B. Rebak, and G. S. Was, "Radiation Damage and Irradiation-Assisted Stress Corrosion Cracking of Additively Manufactured 316L Stainless Steels," *J. Nucl. Mater.,* 513 (2019) 33–44.

[28] G. Meric de Bellefon, K.M. Bertsch, M.R. Chancey, Y.Q. Wang, D.J. Thoma, "Influence of solidification structures on radiation-induced swelling in an additively-manufactured austenitic stainless steel," *J. Nucl. Mater.,* 523 (2019) 291-298.

[29] N. Sridharan, M.N. Gussev, K.G. Field,, "Performance of a ferritic/martensitic steel for nuclear reactor applications fabricated using additive manufacturing,," *J. Nucl. Mater.,* 521 (2019) 45-55.

[30] W. Zhong, N. Sridharan, D. Isheim, K.G. Field, Y. Yang, K. Terrani, L. Tan,, "Microstructures and mechanical properties of a modified 9Cr ferritic-martensitic steel in the as-built condition after additive manufacturing," *J. Nucl. Mater.,* 545 (2021) 152742.

[31] TS Byun, David Collins, Annabelle Le Coq, Tim Lach, Kory Linton, Maxim N Gussev, "Mechanical Properties of Additive Manufacturing 316L Stainless Steel Before and After Neutron Irradiation-FY 2021," Oak Ridge National Laboratory, ORNL/TM-2021/2121 (M2TC-21OR0403032).

[32] TS Byun, TG Lach, YR Lin, DA Collins, K Epps, DT Hoelzer, "Characteristics of oxide-dispersion strengthened alloys produced by high-temperature severe deformation," *J. Nucl. Mater.,* 597 (2024) 155129.

[33] Thak Sang Byun, Maxim N Gussev, Timothy G Lach, "Deformation and Fracture Behavior of Additively Manufactured 316L Stainless Steel," *JOM,* 76 (2024) 362-378.

[34] TS Byun, David Collins, Blane Fillingim, Thomas Feldhausen, Holden Hyer, Yan-Ru Lin, David T Hoelzer, Kevin Hanson, "Downselection and Basic Properties of Additively Manufactured ODS Alloys," ORNL/TM-2023/3033, 2023, August.

[35] Thak Sang Byun, Maxim N Gussev, Nitish Bibhanshu, Timothy G Lach, "Deformation mechanism transition in additively manufactured compositionally graded Fe-base alloys," *JOM,* 74 (2022) 4042-4058.

[36] T. S. Byun, N. Hashimoto, K. Farrell, "Deformation Mode Map of Irradiated 316 Stainless Steel in True Stress-Dose Space," *J. Nucl. Mater.,* 351 (2006) 303–315..

[37] T.S. Byun, S.A. Maloy and J.H. Yoon, "Small Specimen Reuse Technique to Evaluate Fracture Toughness of High Dose HT9 Steel," *Small Specimen Test Tech., ASTM International ,* STP-1576 (2015) 121-141.

[38] B. R. Antoun, C. Alleman, K. De La Trinidad, "Experimental Investigation of Dynamic Strain Aging in 304L Stainless Steel," SAND2018-3171C, Sandia National Laboratory, 2018.

[39] S. N. Monteiroa, F. M. Margem, V. S. Candido, A. Ben-Hur da Silva Figueiredo, "High Temperature Plastic Instability and Dynamic Strain Aging in the Tensile Behavior of AISI 316 Stainless Steel," *Materials Research,* 20 (2017) 506–511.

[40] L. Raman, K. Gothandapani, B.S. Murty , "Austenitic Oxide Dispersion Strengthened Steels: A Review," *Defence Sci. J.,* 66 (2016) 316-322I.

[41] Hiroshi Oka, Masashi Watanabe, Naoyuki Hashimoto, Somei Ohnuki, Shinichiro Yamashita, Satoshi Ohtsuka, "Morphology of oxide particles in ODS austenitic stainless steel," *J. Nucl. Mater. ,* 442 (2013) 164–168.

[42] J.H. Kim, T.S. Byun, D.T. Hoelzer, S.W. Kim, B.H. Lee, "Temperature Dependence of Strengthening Mechanisms in the Nanostructured Ferritic Alloy 14YWT: Part I - Mechanical and Microstructural Observations," *Mat. Sci. Eng. A,* 559 (2013) 101-110.

[43] W.F. Smith, J. Hashemi, Foundations of Materials Science and Engineering, McGraw-Hill, 2006.

[44] T.S. Byun, D.T. Hoelzer, J.H. Kim, S.A. Maloy, "A Comparative Assessment on the Fracture Toughness Behavior of Ferritic-Martensitic Steels and Nanostructured Ferritic Alloys," *J. Nucl. Mater.,* 484 (2017) 157-167.

[45] K. Ma, Z.Y. Liu, K. Liu, X. Grant Chen, B.L. Xiao, Z.Y. Ma, "Enhancement of the strength-ductility relationship for carbon nanotube/Al–Cu–Mg nanocomposites by material parameter optimisation," *Carbon,* 157 (2020) 602-613.

[46] R. Ritchie, "The conflicts between strength and toughness," *Nature Mater.,* 10 (2011) 817–822.

[47] R.O. Ritchie, J.F. Knott, J.R. Rice, "On the relationship between critical tensile stress and fracture toughness in mild steel," *J. Mech. Phys. Solids,* 21 (1973) 395-410.

[48] R.H. Jones, C.A. Lavender, M.T. Smith, "Yield strength-fracture toughness relationships in metal matrix composites," *Scripta Metall.,* 21 (1987) 1565-1570.